Photoacoustics 21 (2021) 100222

Contents lists available at ScienceDirect

Photoacoustics

journal homepage: www.elsevier.com/locate/pacs

Research article

A three-dimensional modeling method for quantitative photoacoustic breast imaging with handheld probe

Tao Han [a], Meng Yang [b], Fang Yang [c], Lingyi Zhao [a], Yuxin Jiang [b], Changhui Li [a,*]

[a] Biomedical Engineering Department, Peking University, Beijing, 100871, China
[b] Department of Ultrasonography, Peking Union Medical College Hospital, Beijing, 100730, China
[c] Mindray Bio-Medical Electronics Co., Ltd., Shenzhen, 518057, China

ARTICLE INFO

Keywords:
Photoacoustic computed tomography
Ultrasound imaging
Multi-modality imaging
Three dimensional fluence compensation
Quantitative photoacoustic breast imaging

ABSTRACT

By providing complementary functional information, photoacoustic (PA) breast imaging based on the handheld ultrasound (US) probe has demonstrated promising potential for breast cancer diagnosis. However, the quantitative PA imaging primarily relies on the knowledge of the optical fluence distribution in the three-dimensional (3D) heterogeneous breast tissue. Previous studies based on the handheld system generally provided two-dimensional (2D) B-scan results, which contains limited anatomical information of the tissue and the lesion. This study proposed a method to perform 3D modeling of the photon transportation for dual-modality PA/US system based on the local 3D breast anatomical information by scanning US probe. Then the calculated optical fluence distribution can be used for PA imaging. Our phantom and clinical pilot study results demonstrated that this method has potential to improve the accuracy of the quantitative PA breast imaging, and it can also be used in other clinical implementations.

1. Introduction

Photoacoustic imaging (PAI) is an emerging technique that constructs images of biological tissues based on the contrast which is determined by the characteristics of their optical absorptions [1]. Since the hemoglobin in blood has strong and unique optical absorption in comparison to other tissues, blood vessels are considered as superior endogenous targets for imaging. Therefore, PAI has been utilized in clinical implementations to assist with diseases diagnosis when abnormal vasculature behavior is observed, especially in cancer diagnosis [2,3]. Breast cancer is a world-wide threat that takes up 30 % of all new cancer diagnosis among women [4], hence much attentions are attracted to the PA breast imaging [5]. Among many developed PA breast imaging systems, the handheld PA/US dual-modality system based on the clinical US system is preferred by physicians due to its familiarity [6]. Besides, the traditional B-scan ultrasound (US) imaging can also provide important complementary anatomical information [7]. Up to now, several PA/US handheld systems have been developed for clinical study and the results showed great potential in breast cancer diagnoses [8–12].

One of the important physiological parameters for breast cancer is the oxygen saturation (SO_2), which can be derived from quantitative PA imaging based on the spectral differences in optical absorption between the oxygenated and the de-oxygenated hemoglobin [13]. Since the PA signal is proportional to the multiplication of the tissue optical absorption coefficient with the local optical fluence and the Grüneisen parameter, the quantitative PA breast imaging requires compensation for the fluence difference at different light wavelengths. However, it becomes a very challenging job because of the high heterogeneity in living tissue that heavily increases the complexity in fluence distribution. Several approaches are being explored, including the direct calculation of the fluence based on numerically solving the radiative transfer equation [14–16], spectral unmixing methods [17,18], and most recently machine learning algorithms [19–21]. In this work, we employed the first approach.

The optical fluence could be calculated once the anatomical structure in human breast with corresponding optical properties were known. For instance, the finite element forward model is used for the optical fluence compensation [22], and several researches employed this way for the handheld PA/US 2D imaging [23,24]. However, the breast tissue, especially when there is a lesion, has an optically heterogeneous 3D structure, leading to non-negligible variation of optical properties for different types of normal tissues and lesions. Therefore, the lack of important 3D morphology of the tissue in 2D imaging, the accuracy of

* Corresponding author.
E-mail address: chli@pku.edu.cn (C. Li).

https://doi.org/10.1016/j.pacs.2020.100222
Received 30 September 2020; Received in revised form 10 November 2020; Accepted 12 November 2020
Available online 28 November 2020

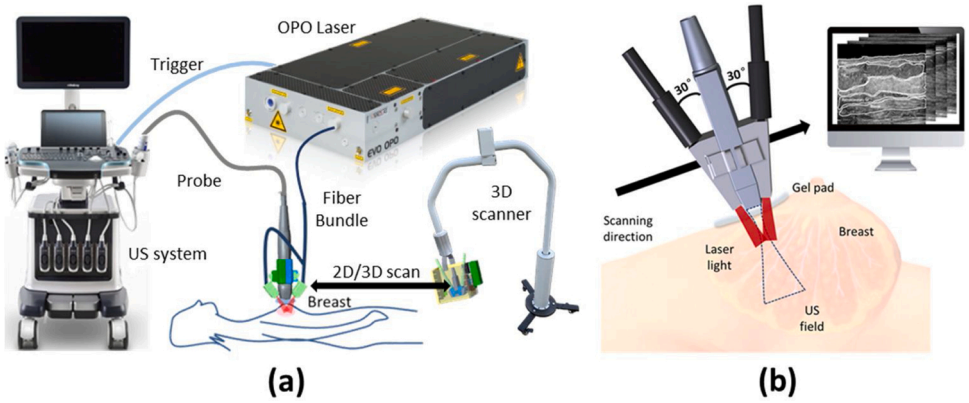

Fig. 1. (a) A diagram of the US/PA dual-modality system; (b) An illustration of US/PA dual-modality probe setup, the scanning process will produce a series of B-scan images along the scanning direction.

the optical fluence compensation would be affected.

In this study, based on a dual-modality PA/US system that used a linear probe, we proposed a 3D modeling method to calculate the optical fluence distribution, and then used this information to compensate the PA imaging results. In this method, we scanned a US probe over the entire suspicious breast lesion, from where different types of tissues (such as skin, adipose tissue, and fibroglandular tissue), as well as the tumor, were identified based on US B-scan serial images. Their optical properties were assigned accordingly, which enabled personalized 3D modeling of human breasts. We quantitatively studied fluence compensation model on heterogeneous phantom and breast tumor patients, and calculated SO_2 with and without fluence compensation. Our results demonstrated 3D modeling could improve the accuracy of quantitative PA breast mapping.

2. Methods and material

2.1. PA/US dual-modality imaging system

A clinical US system (Resona7, Mindray Bio-Medical Electronics, Shenzhen, China), which is connected with a 192 elements linear probe (L9-3U, Mindray Bio-Medical Electronics, Shenzhen, China) of 5.8 MHz-central-frequency was modified to perform US/PA dual-modality imaging which provides FOV of 4.4 cm × 5 cm. The laser source is an optical parameter oscillation (OPO) laser (SpitLight EVO 200, InnoLas Laser GmbH, Krailling, Germany) with a repetition rate of 10 Hz. The laser was delivered via a one-two fiber bundle (made by CeramOptec GmbH, Bonn, Germany), and the two bundle terminals were mounted on both sides of the US handheld probe to illuminate the tissue at an incident angle of 30° for less direct illumination under the probe. This incident angle is refracted to 21° after the light entering a transparent custom-made ultrasound gel pad of 1.0 cm thickness from the air. The refractive-index-matched boundary condition was employed between gel pad and tissue. To measure the SO_2, we used two wavelengths, 750 nm and 830 nm, for the PA phantom and human breast imaging. The measured fluence onto the skin surface from each laser beam is 10 mJ/cm^2, which is within the safety limit according to the ANSI standard. The output energy of each laser pulse is constantly monitored and was used to compensate the PA results via normalization. Fig. 1(a) shows the setup of the US/PA dual-modality system. A zoomed-in diagram illustrates the dual-modality hand-held probe and the scanning process, as shown in Fig. 1(b).

During the clinical pilot study, the physician first held the handheld probe to locate the tumor by US, then the probe was mounted onto a scanner which automatically conveyed the probe at a speed of 0.1 cm/s for a total 4.0 cm range, covering the entire suspicious lesion region found by US. The gel pad was put between the scanner and patient to reduce the unwanted PA signal at the probe surface. Physician applied force on the gel pad to flatten the human breast surface to avoid surface tissue deformation when scanning the probe. Since we only applied slight force, it won't cause obvious tissue deformation.

Our study protocol was approved by the institutional ethics committee of Peking Union Medical College Hospital. All research was performed in accordance with relevant regulations. Written informed consent was obtained from all participants. Biopsy and surgical resection were performed on all the enrolled patients with pathological diagnoses. Frozen section and paraffin section results confirmed that the first patient had breast fibroadenoma while the second patient had breast papilloma.

2.2. Theory of blood oxygen saturation correction by optical fluence compensation

The initial pressure $\boldsymbol{p}_0$ generated by PA effect is proportional to the local absorbed photon energy density $\boldsymbol{A}_e$ (J/m^3), which is described by [Eq. (1)]:

$$\boldsymbol{p}_0 = \Gamma \eta_{th} \boldsymbol{A}_e, \tag{1}$$

where Γ is the Grüneisen parameter which is a temperature sensitive dimensionless parameter, η_{th} is the percentage of the absorbed photon energy that is converted into heat. The absorption coefficient μ_a (cm^{-1}) has the relationship to the $\boldsymbol{A}_e$, as follows,

$$\mu_a(\boldsymbol{\lambda}, \boldsymbol{r}) = \frac{\boldsymbol{A}_e(\boldsymbol{\lambda}, \boldsymbol{r})}{\boldsymbol{F}(\boldsymbol{\lambda}, \boldsymbol{r})} \propto \frac{\boldsymbol{p}_0(\boldsymbol{\lambda}, \boldsymbol{r})}{\boldsymbol{F}(\boldsymbol{\lambda}, \boldsymbol{r})}, \tag{2}$$

where $\boldsymbol{F(\lambda,r)}$ (J/m^2) is the optical fluence that is used to describe the local density of the laser photons. Since the blood vessel absorption coefficient depends on the concentrations of both oxygenated hemoglobin and deoxygenated hemoglobin, the SO_2 can be calculated by measuring PA signals from at least two wavelengths [25].

Because the optical parameters in different tissue types are also wavelength dependent, local optical fluence compensation need to be calculated at corresponding wavelengths. To assess the effectiveness of fluence compensation later, we defined the ΔSO_2 representing the SO_2 difference between compensated (cSO_2) value based on our 3D modeling and the un-compensated (uSO_2) value which is derived directly from the 2D PA/US imaging results:

$$\Delta SO_2 = uSO_2 - cSO_2 \tag{3}$$

As a simpler approximate compensation approach, the bulk tissue is also sometime assumed to be an optically homogenous with uniform background absorption and scattering properties (with spectral difference). For comparison with our method, we also define the hSO_2 as

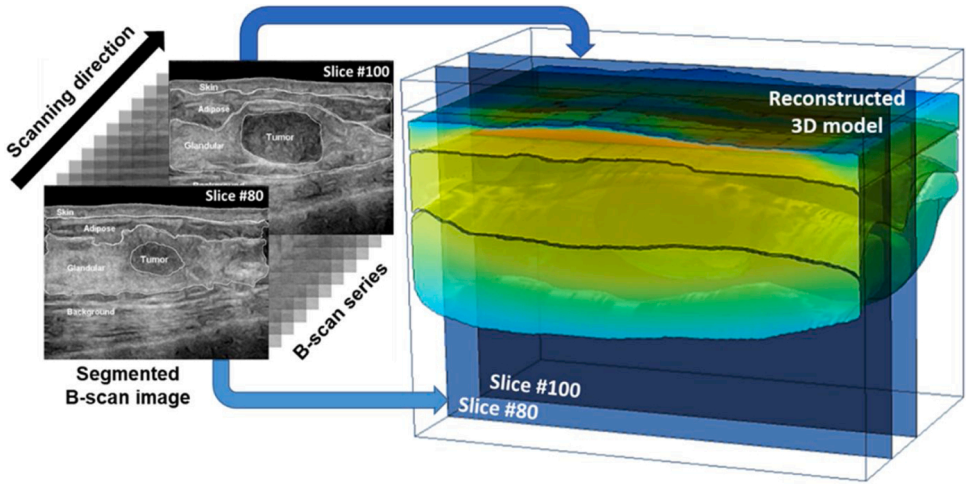

Fig. 2. The 3D breast model is reconstructed from a series of US B-scan images in which two slices are selected to further explain the reconstruction mechanism.

compensated SO_2 value when breast tissue or phantom is considered as 3D homogeneous material. The difference between hSO_2 and cSO_2 is therefore depending on whether tissue or phantom is compensated based on homogeneous model (hSO_2) or heterogeneous model (cSO_2).

2.3. 3D modelling of photon transportation in breast tissue

According to the real conditions, the illumination pattern is modelled as two identical rectangles by the size of 4.7 cm × 0.8 cm located at 0.93 mm below skin surface where photons have passed one transport mean free path. For 3D study in which the probe scans, the lateral position of the light source will move together with the probe. The fluence calculation is based on the light diffusion model which demands 3D breast structure. In this study, we reconstructed the 3D breast model through a series of 2D US B-scan slices. Then, we can identify different types of tissues (i.e. skin, adipose tissue, and fibroglandular tissue) and tumor according to their US characteristics and anatomical features to do image segmentation. The identified tumor and tissues were segmented separately and fused into a complete 3D breast model. In this pilot study, we only chose patient whose tumor has a distinguished boundary in US imaging to avoid ambiguity and the segmentation is done manually under the guidance from experienced physicians. A diagram of this process is shown in Fig. 2, where two B-scan slices are selected to illustrate the 3D reconstruction mechanism.

After segmentation, the 3D model is constructed by integrating slices with tumor and normal tissues individually using the function 'loft' in the COMSOL Multiphysics (COMSOL Inc., Stockholm, Sweden), and then optical parameters of each segmented region are imported to the corresponding domain, where we can set optical diffusion equations and boundary conditions to calculate the optical fluence. The COMSOL solves the diffusion equation in the breast tissue regime and the source is quantified using current density S at the illumination site [26]:

$$\begin{cases} -\frac{1}{\mu_{eff}^2}\nabla^2\boldsymbol{\Phi}(\boldsymbol{\lambda},\boldsymbol{r}) + \boldsymbol{\Phi}(\boldsymbol{\lambda},\boldsymbol{r}) = 0 \\ \frac{1}{\mu_{eff}^2}\nabla\boldsymbol{\Phi}(\boldsymbol{\lambda},\boldsymbol{r})\cdot\mathbf{n} = S(r) \end{cases} \tag{4}$$

where $\boldsymbol{\Phi}$ is the optical fluence, $\mathbf{n}$ is a unit vector normal to the illumination spot and the effective attenuation coefficient μ_{eff} is defined as:

$$\mu_{eff} = \sqrt{3\mu_a(\mu_a + \mu_s')} \tag{5}$$

where μ_a and μ_s' are the absorption coefficient and the reduced scattering coefficient, respectively. To build a breast model that based on the anatomical structure, we allocate specific μ_{eff} to each segmented tissue for the simulation of photon distribution.

Table 1
Optical parameters of different tissue layers [27–31].

Tissue type	Wavelength(nm)	μ_a (cm^{-1})	μ_s' (cm^{-1})	μ_{eff}(cm^{-1})
Skin	750	0.63	20.8	6.36
	830	0.59	18.4	5.8
Adipose tissue	750	0.036	11	1.09
	830	0.034	10.2	1.02
Fibroglandular tissue	750	0.084	12.8	1.8
	830	0.096	11.2	1.81
Background	750	0.03	11	1.01
	830	0.038	10.4	1.09
Tumor	750	0.12	8.3	1.74
	830	0.13	7.2	1.69

In this study, we used two wavelengths (750 nm and 830 nm) for the quantitative PA imaging. The optical properties of skin, adipose tissue, fibroglandular tissue, tumor, and background tissues at these two wavelengths was used according to previous reported literature studies [27–31], as listed in Table 1. The background tissues cover the regions outside the segmented tissues (see Fig. 2). The optical parameters that describe the background tissue comes from literature when the optical properties of human breast are measured *in vivo* and the entire human breast is considered as homogeneous material.

2.4. Tissue mimicking phantom

Since it is still challenging to know the actual SO_2 values in human breast vessels via non-invasive method, so we designed a phantom study to evaluate the performance of our method. The breast tumor mimicking phantom is in ellipsoidal (2cm × 1.4cm × 1.4cm) shape, which consists of 2 % agar (Sigma-Aldrich, Missouri, United States), 1 % intralipid (KeLun Industry Group, Szechuan, China) and 0.005 % indocyanine green (Fisher Scientific, Pittsburgh, United States). The agar to make the tumor phantom was first heated to 100 ℃ which is above its melting point, then intralipid and indocyanine green were added to the solution when the temperature was dropping to 50 ℃. The mixed solution was poured into an ellipsoidal mold for solidification. To mimic the blood vessel, we used a silicon tube (outer diameter 1mm, inner diameter 0.5mm) which pierced through the ellipsoid along its long axis and hung horizontally at 1.6 cm depth. Following the reported procedure of ref [32], the bulk breast tissue phantom is consisted of 0.1 % TiO_2 (Sigma-Aldrich, Missouri, United States) and gel wax (Yaley

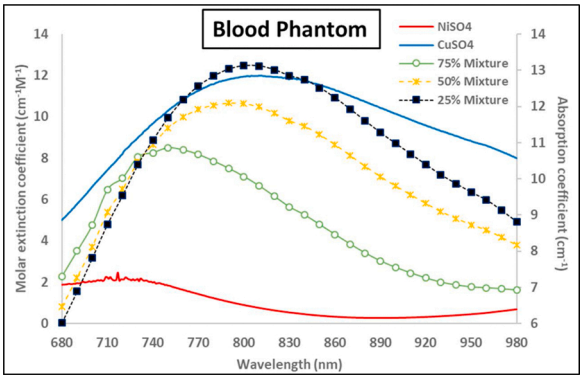

Fig. 3. Optical parameters of the pseudo-blood phantom: red line and blue line are the molar extinction coefficients of $NiSO_4$ and $CuSO_4$; green line with hollow dots, yellow dashed line with crosses and black dotted line with boxes are the absorption coefficient of 75 %, 50 % and 25 % pseudo-SO_2 blood phantom, respectively. (For interpretation of the references to colour in this figure legend, the reader is referred to the web version of this article).

Enterprises, California, United States). The gel wax was heated to a liquid state at 170 ℃ and put into a sonicator (KQ3200ES, KunShan Ultrasonic Instruments, JiangSu, China) which sustained a water bath at 100 ℃. TiO_2 was then added into the gel wax solution during sonication for mixing and degassing. When there were no TiO_2 particles or bubbles visualized, the mixed solution was slowly poured into the acrylic container at 70 ℃.

Because we were not accessible to instruments to measure SO_2 of real blood sample, so we used pseudo-blood material instead according to ref [33]. The pseudo blood is a mixture of $NiSO_4$ (pseudo-oxygenated hemoglobin) and $CuSO_4$ (pseudo-deoxygenated hemoglobin) solution. Therefore, the value of pseudo-SO_2 is calculated using the molar concentration of $NiSO_4$ divided by the summation of the molar concentrations of both $NiSO_4$ and $CuSO_4$. Three distinct pseudo-SO_2 values of blood mimicking phantoms were selected for the experiment, which are 75 %. 50 % and 25 % respectively. The absorption spectrum of those two chemicals were measured using a spectrophotometer (UV-3600 Plus, SHIMADZU, Kyoto, Japan), as shown in Fig. 3 in red and blue lines, and the absorption coefficient of the mixture 75 %, 50 % and 25 % are represented by green line with hollow dots, yellow dashed line with crosses and black dotted line with boxes, respectively.

The experiment setup is shown in Fig. 4(a) and (b). The US probe was first held vertically to locate the ellipsoid and the maximum longitudinal section of the silicon tube via US imaging, and then kept the probe steady during the experiment. Lasers with 750 nm and 830 nm wavelengths were employed for PA imaging. After the PA/US dual imaging, the phantom was dissected to measure the actual size and position of the ellipsoid, which is used for 3D reconstruction of the anatomical structure. The optical parameters that involved in the phantom model are shown in Table 2.

3. Results

3.1. Phantom study

Fig. 5(a) shows the results of the PAI imaging of the phantom with 75 % pseudo-SO_2 level at 750 nm wavelength. The white dashed contour line represents the boundary of the tumor. The corresponding fluence distribution of the phantom is modelled and presented in Fig. 5(b) at 750 nm wavelength. When 75 % pseudo-SO_2 solution was in the tube, the measured pseudo-uSO_2 (without fluence compensation) and the pseudo-cSO_2 (with fluence compensation) mapping are shown in the upper section of Fig. 5(c). The exhibited region enclosed in the red dashed box in Fig. 5(c) is corresponding to the same region in the red dashed box in Fig. 5(a). The averaged pseudo-uSO_2 and pseudo-cSO_2 values along the vessel are presented in dashed blue line and solid black line in the lower section of Fig. 5(c). According to the SO_2 mapping, the pseudo-cSO_2 is overall larger than the uncompensated counterpart. We also calculated the probability density function of pseudo-uSO_2 (purple bars) and pseudo-cSO_2 (green bars) for 75 %, 50 % and 25 % pseudo-SO_2 level of the area inside the red dashed box. The distributions of their probability density functions are introduced by histogram shown in Fig. 5(d–f). The red and blue lines in Fig. 5(d–f) are the normal fitting curve to the probability density function of pseudo-uSO_2 and pseudo-cSO_2, respectively. In Fig. 5(d), The red fitting curve is centered at 70.0 % and the blue fitting curve is centered at 74.0 % when the actual pseudo-SO_2 value is 75 %. In Fig. 5(e), the pseudo-uSO_2 is centered at 43 % while the pseudo-cSO_2 is centered at 51 % for 50 % pseudo-SO_2 value. Finally, for the 25 % pseudo-SO_2 value, the mean pseudo-uSO_2 is 21 % and the mean pseudo-cSO_2 is 24 %. Two more results with different pseudo-SO_2 values (0% and 100 %) are provided in the supplementary note 1 (Fig. S.1), and they both show the increase in accuracy. Therefore, the phantom study results indicate that the fluence compensation based

Table 2
Optical parameters of phantom [32,34–36].

Phantom	Wavelength(nm)	μ_a (cm^{-1})	μ_s' (cm^{-1})	μ_{eff}(cm^{-1})
Substrate	750	0.02	5.5	0.57
	830	0.02	5	0.55
Ellipsoid	750	0.09	11	1.73
	830	0.07	10	1.52

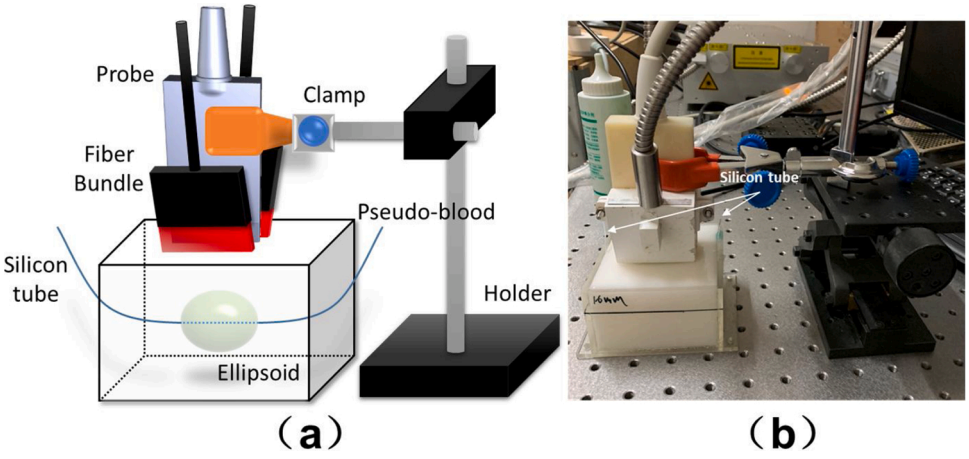

Fig. 4. (a) A schematic diagram of the phantom experiment setup; (b) A photograph of actual setup during phantom experiment.

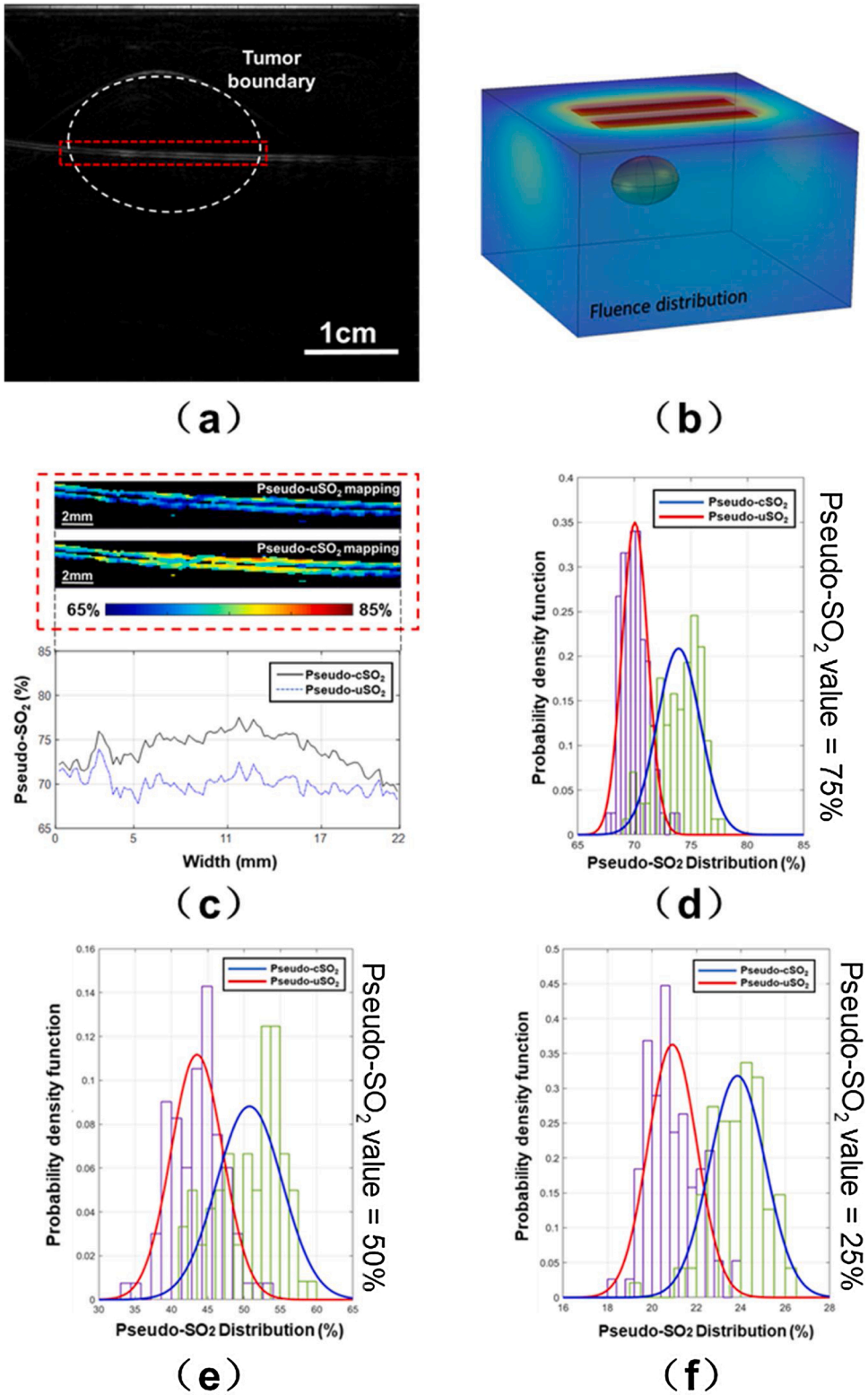

Fig. 5. (a) Normalized PA signal of the phantom at 750 nm wavelength (75 % actual pseudo-SO_2 value); (b) Fluence distribution of 3D model at 750 nm wavelength; (c) upper: Pseudo-uSO_2 and pseudo-cSO_2 mapping inside the same red dashed box in (a); lower: the averaged pseudo-uSO_2 and pseudo-cSO_2 values distribution along the horizontal vessel (75 % actual pseudo-SO_2 value); (d-f) The purple and green bars are the probability density function of pseudo-uSO_2 and pseudo-cSO_2 distribution of 75 %, 50 % and 25 % actual pseudo-SO_2 values. The red and blue lines are normal fitting curve to pseudo-uSO_2 and pseudo-cSO_2 distribution, respectively. (For interpretation of the references to colour in this figure legend, the reader is referred to the web version of this article).

on 3D modeling would increase the measurement accuracy.

3.2. Pilot clinical study

We also investigated the effect of fluence compensation on SO_2 measurement on one healthy volunteer and two patients with benign tumors. As aforementioned, for the patient study, the physician first located the suspicious lesion via routine US examination, then the probe was mounted on a scanner to scan over the lesion. We first constructed the 3D breast modeling based on US B-scan results. Then the optical fluence can be calculated. For the healthy volunteer, Fig. 6(b) represented the imaging result at 785 nm wavelength when the probe was at the center position during scanning. We chose a 2.5cm × 2.0cm ROI that centered at 1.6 cm depth to show the mapping of uSO_2 (Fig. 6a), cSO_2

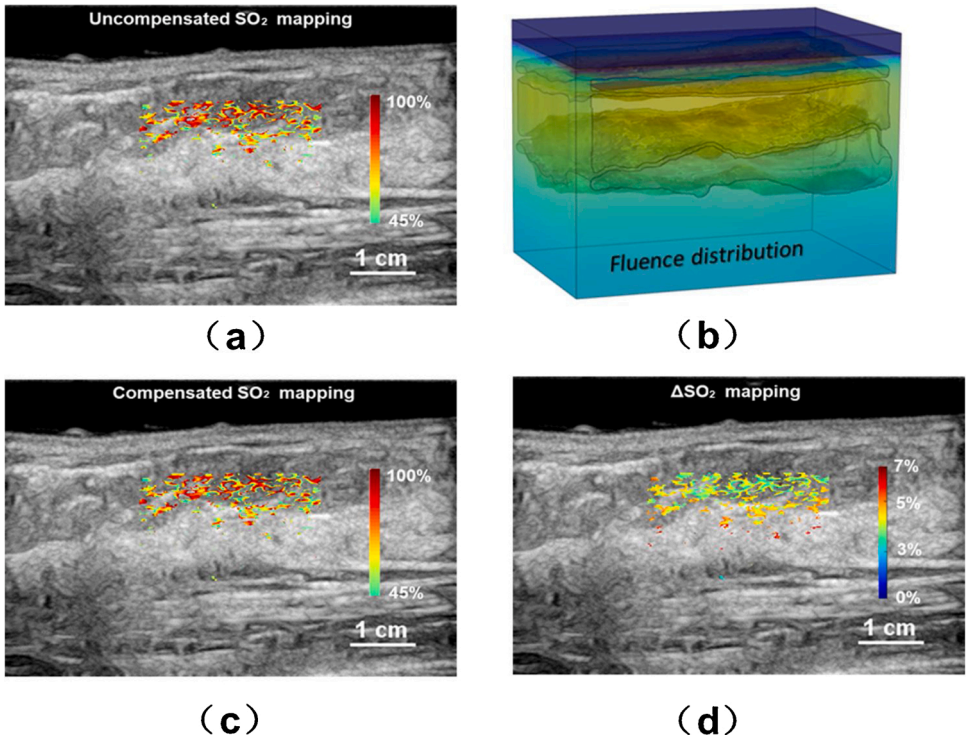

Fig. 6. Study results for the healthy volunteer. (a) The uncompensated SO2 distribution; (b) the 3D modeling of the fluence distribution; (c) the compensated SO2 distribution based on the 3D modeling; (d) the ΔSO_2 mapping.

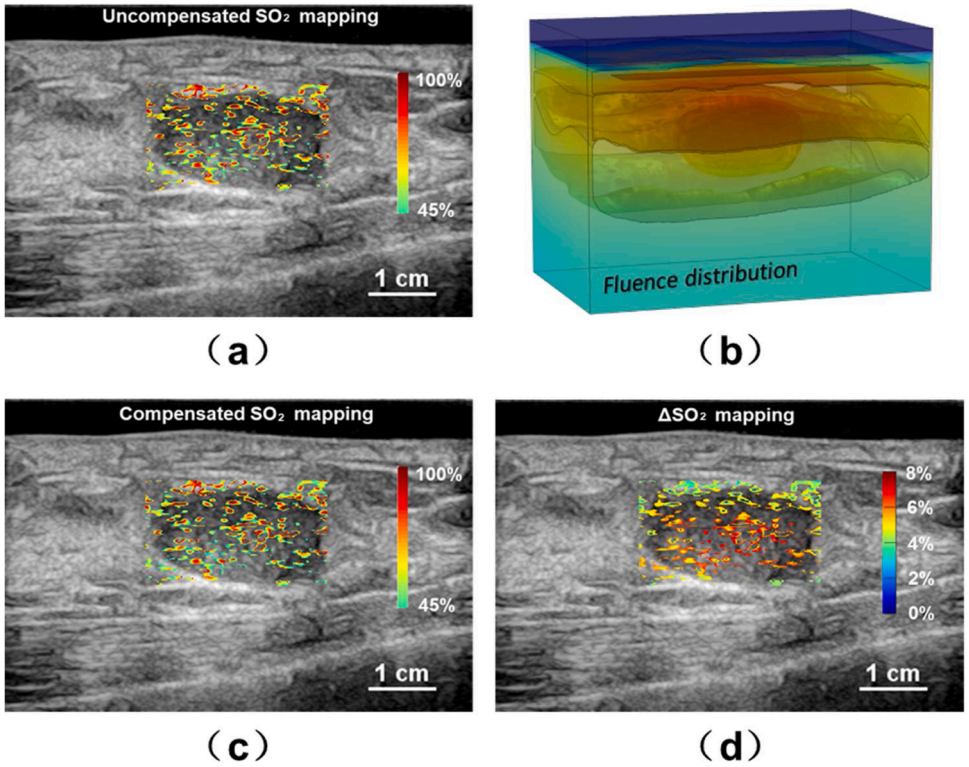

Fig. 7. Study results for the first patient. (a) The uncompensated SO2 distribution; (b) the 3D modeling of the fluence distribution; (c) the compensated SO2 distribution based on the 3D modeling; (d) the ΔSO_2 mapping.

(Fig. 6c) and ΔSO_2 (Fig. 6d), respectively. The ΔSO_2 value is primarily around 3% in superficial region and over 5% in deeper area.

For the breast tumor cases, the tumors in this study have fairly regular shapes with their center positions situated in the fibroglandular layer at about 1.6 cm below skin surface. The majority of breast tumors are located in this layer where blood vessels are relatively abundant. The

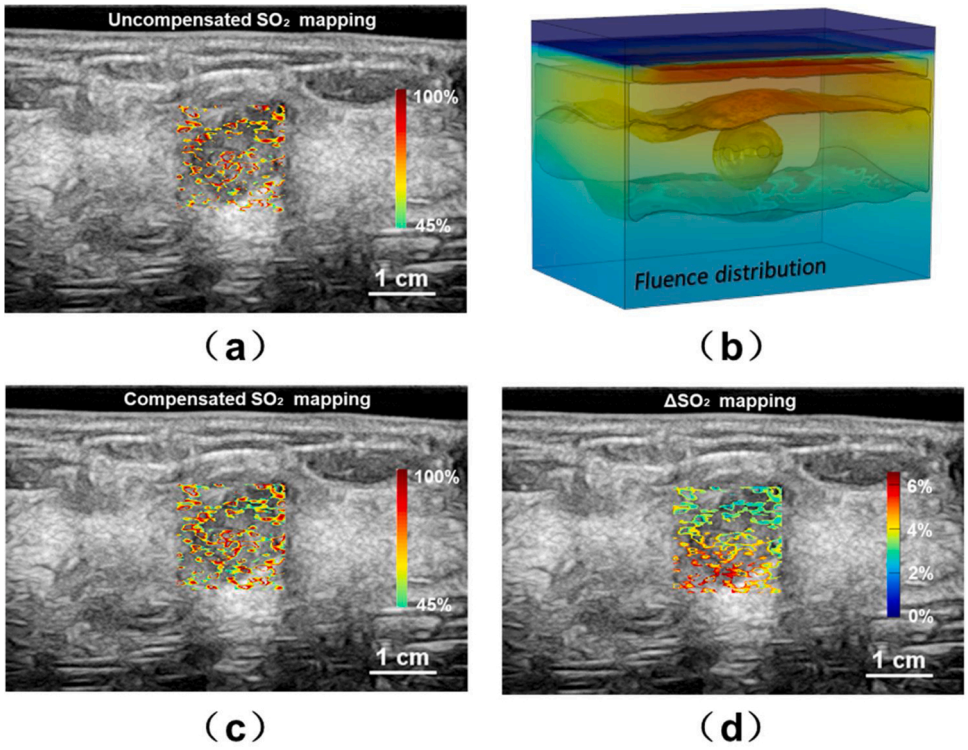

Fig. 8. Study results for the second patient. (a) The uncompensated SO2 distribution; (b) the 3D modeling of the fluence distribution; (c) the compensated SO2 distribution based on the 3D modeling; (d) the ΔSO_2 mapping.

first patient (right breast) has a tumor size 2.0 cm × 1.4 cm × 1.1 cm centered at 1.58 cm in depth while the second patient (left breast) has a smaller one with a size of 1.1 cm × 0.9 cm × 0.9 cm centered at 1.59 cm in depth. For both patients, we chose the ROI of ΔSO_2 distribution in a rectangular box that concentric with the tumor while each side of the box is 1.0 mm broader than the tumor. The tumor and its surrounding area we presented are the most interested region by physicians.

The uSO_2 map of the first patient is shown in Fig. 7(a) without the optical fluence compensation. As aforementioned, a 3D local breast model with the tumor can be constructed based on US B-scan results, and the corresponding fluence distribution map exhibited under 785 nm laser illumination is shown in Fig. 7(b). Fig. 7(c) and (d) showed the cSO_2 map and the ΔSO_2 mapping, respectively. It can be seen that the compensation based on 3D model can rectify the absolute SO_2 value up to 7.8 % (58.24 % in cSO_2 and 65.32 % in uSO_2) at the central areas of the tumor and 4% in the surrounding areas. This correction would be important for physicians to assess the blood SO_2 level inside/around the tumor.

Fig. 8(a–d) shows the results for the second patient whose tumor size is smaller. The ΔSO_2 mapping indicates the most difference is no longer located at the central area of tumor but rather distributed along the top and bottom surface. The cSO_2 around bottom left corner is 6% lower than the uSO_2 value while 3% lower than the uSO_2 value near the top surface.

3.3. Comparison with homogeneous model

To further validate the effectiveness of our method, we compared our method to a 3D compensation method in which the breast tissue or phantom are considered as a homogeneous scattering material. As defined earlier, we use hSO_2 minus cSO_2 values to show the differences between those two methods. Fig. 9(a–c) shows the comparison of pseudo-uSO_2, pseudo-cSO_2 and pseudo-hSO_2 values in the phantom study at 75 %, 50 % and 25 % pseudo-SO_2 level, respectively. The horizontal line in the middle of the black boxes in Fig. 9(a–c) represents the mean value of the pseudo-SO_2 in the silicon tube. The top and bottom edge of the black box represents the standard deviation (S.D.) of the pseudo-SO_2 values. Upper and lower error bars represent maximum and minimum pseudo-SO_2 values. From the results, although the pseudo-hSO_2 values can be slightly more accurate by 1–2 % than the uncompensated results, our method significantly increased the accuracy. Fig. 9 (d–e) shows the mappings of SO_2 differences between hSO_2 and cSO_2 values of the first and the second patient. The SO_2 differences between these two methods are more significant at deeper tumor region in the human breast.

4. Discussions and conclusion

In this work, we developed a method to locally compensate the spectral fluence difference for quantitative PA breast imaging. Based on a serial of US B-scan results, the reconstructed 3D anatomical structure, together with corresponding spectral-dependent optical parameters, can be used to calculate the optical fluence, which is essential for the quantitative PA imaging, such as the SO_2 mapping. The phantom study indicated that our method could increase the accuracy of the SO_2 mapping. For pilot clinical study, we imaged two tumors with different size. According to the ΔSO_2 mapping from Figs. 6–8, the magnitude of the compensation indicates non-negligible influence of optical fluence compensation by 3D modeling on quantitative PA breast imaging. Meanwhile, to effectively increase the SO2 accuracy with our method, it is desired to have accurate optical parameters of different tissue types for each patient.

We also compared the results of our 3D structure-based compensation with 3D model where only a homogenous tissue is considered for both human and phantom cases. In Fig. 9(a–b), up to 10 % SO_2 differences between two methods can be observed in human cases especially in deeper regions. For the phantom study results shown in Fig. 9(c–e), although the difference between two methods is less significant than human cases, the compensation using our method is still more effective than homogeneous 3D compensation. The pseudo-cSO_2 values are not

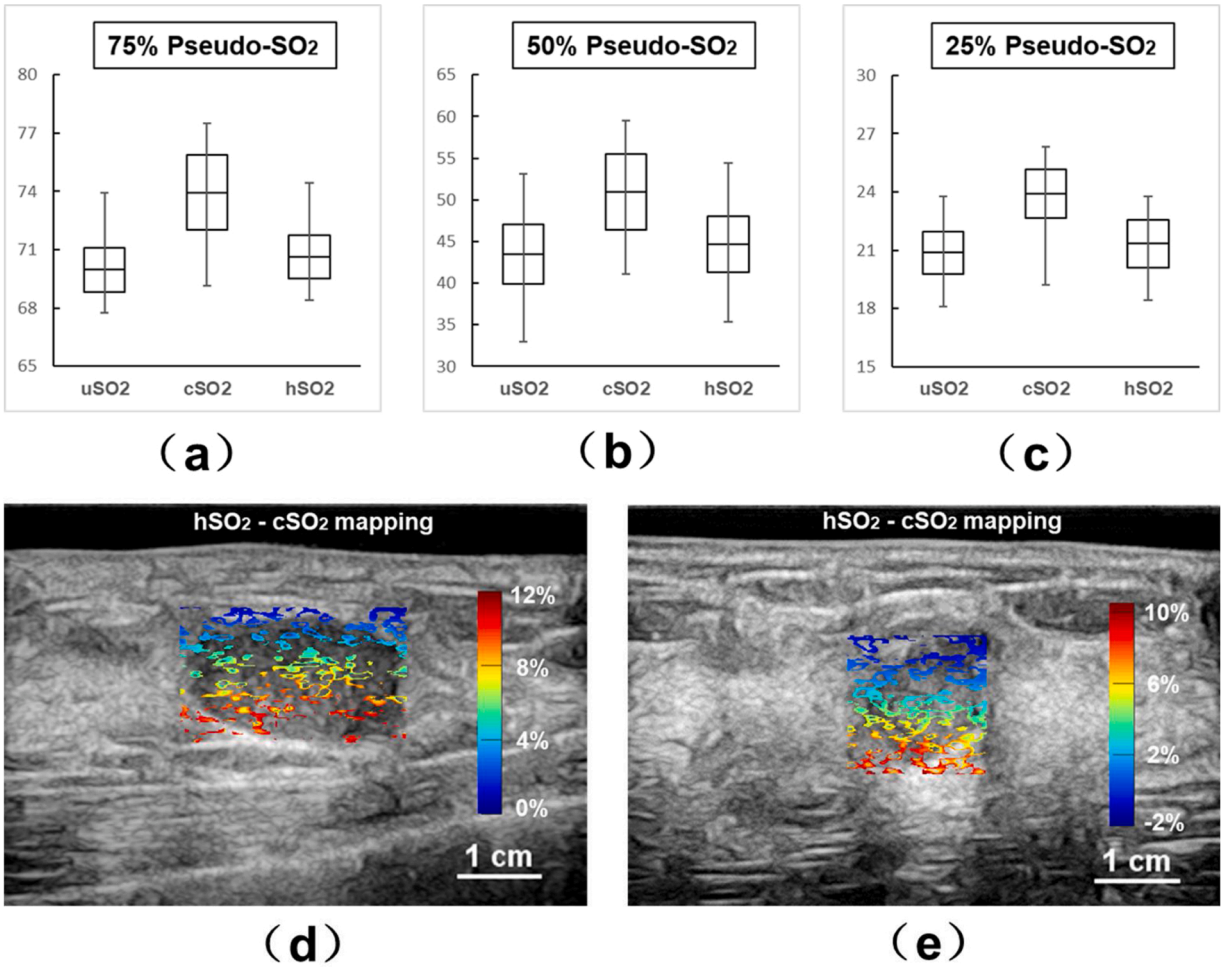

Fig. 9. (a-c) pseudo-uSO_2, pseudo-cSO_2 and pseudo-hSO_2 values in the phantom study at 75 %, 50 % and 25 % actual pseudo-SO_2 levels. Mean value is represented by horizontal line in the black box; S.D. values are represented by the top and bottom edges of the black box; error bars indicate maximum and minimum values of the pseudo-SO_2 values; (d-e) Difference mapping between pseudo-hSO_2 and pseudo-cSO_2 values for the first and second patients.

only closer to the actual pseudo-SO_2 values, but also showing more potentials of improvement than pseudo-hSO_2 compare to pseudo-uSO_2 values.

However, the accuracy of the calculated SO_2 highly depends on the imported optical parameters of different tissue types in the 3D modeling. In practice, these parameter values vary from person to person. Therefore, finding a robust method to accurately measure these personalized optical parameters is crucial for the implementation of our method (supplementary note.2). In addition, the diffusion approximation used in our model requires the condition that there is no bulky strong optical absorption regions. In our clinical studies, the subjects are either healthy or earlier stage benign tumor, which satisfied this condition. However, for breast cancers of later stage, prominent angiogenesis or necrosis tissue inside lesion may contain strong optical absorbers, which will potentially impair the effectiveness of diffusion approximation. Besides, tissue segmentation is also a crucial factor which needs to be assured by experienced physicians.

We also evaluated the effect of breathing motion which is shown in the supplementary video. According to the clinical imaging results shown in Fig. 7, the thickness of the imaged human breast is over 4 cm from the skin surface to the chest wall. Based on the mechanical properties of the soft tissue, which is not a rigid matter, the breathing motion will cause more serious tissue deformation in the deeper region close to the chest wall. While, both tumors in this study are located primarily within 2 cm below the skin surface. We didn't notice prominent tissue deformation around the tumor. Therefore, the breathing motion can be neglected in our reported cases.

Besides, several future works should be carried out. First, more clinical study cases are needed, including more types, size, and locations of breast tumor/cancer to provide a comprehensive statistical analysis for clinical use. In our previous work, the un-compensated results have already showed prominent differences in statistical SO_2 for benign and malignant breast tumors [37]. Second, the whole modelling process is still time-consuming by manually segmentation of tumor boundaries from US results. We expect to have more clinical cases, then we can use machine learning to speed up the segmentation. Third, we will quantitatively evaluate the effectiveness of our method on new locations where a large artery can be identified in the ROI, so we can use the SO_2 value as reference. Finally, we will improve the sensitivity of our imaging system. At this moment, there are still SO_2 variations that can be observed in the red dashed box in Fig. 5(c). Although there are several reasons contributing to this phenomenon, including the non-uniform phantom manufacturing, low SNR, and strong optical absorption inside the "phantom blood", we believe the relatively low SNR (or contrast to noise ratio (CNR) $\approx$ 9.1 in the reconstructed images) is the primary cause.

Finally, by developing this diffusion model, we are aiming to provide a promising tool for clinical use. We expect our method could increase the accuracy of local SO_2 value which can help physicians to diagnosis of breast tumors. Moreover, this method can be straightforwardly implemented to other clinical PA imaging studies, such as the thyroid imaging.

Declaration of Competing Interest

We declare that we have no financial and personal relationships with other people or organizations that can inappropriately influence our work. there is no professional or other personal interest of any nature or kind in any product, service and/or company that could be construed as influencing the position presented in, or the review of, the manuscript entitled “A three-dimensional modeling method for quantitative photoacoustic breast imaging with handheld probe”.

Acknowledgements

Funding: The National Key Research and Development Program from the Ministry of Science and Technology of the People’s Republic of China [No. 2017YFE0104200]; Beijing Natural Science Foundation [JQ18023]; the National Natural Science Foundation of China [No. 81421004, 61971447]; and the National Key Instrumentation Development Project from the Ministry of Science and Technology of the People’s Republic of China [No. 2013YQ030651].

Appendix A. Supplementary data

Supplementary material related to this article can be found, in the online version, at doi:https://doi.org/10.1016/j.pacs.2020.100222.

References

[1] L.V. Wang, S. Hu, Photoacoustic tomography: in vivo imaging from organelles to organs, Science 335 (2012) 1458–1462, https://doi.org/10.1126/science.1216210.
[2] F. Knieling, C. Neufert, A. Hartmann, J. Claussen, A. Urich, C. Egger, M. Vetter, S. Fischer, L. Pfeifer, A. Hagel, C. Kielisch, R.S. Görtz, D. Wildner, M. Engel, J. Röther, W. Uter, J. Siebler, R. Atreya, W. Rascher, D. Strobel, M.F. Neurath, M. J. Waldner, Multispectral optoacoustic tomography for assessment of Crohn’s disease activity, N. Engl. J. Med. 376 (2017) 1292–1294, https://doi.org/10.1056/NEJMc1612455.
[3] G. Diot, S. Metz, A. Noske, E. Liapis, B. Schroeder, S.V. Ovsepian, R. Meier, E. Rummeny, V. Ntziachristos, Multispectral optoacoustic tomography (MSOT) of Human Breast Cancer, Clin. Cancer Res. 23 (2017) 6912–6922, https://doi.org/10.1158/1078-0432.CCR-16-3200.
[4] R.L. Siegel, K.D. Miller, A. Jemal, Cancer statistics, 2018, CA Cancer J. Clin. 68 (2018) 7–30, https://doi.org/10.3322/caac.21442.
[5] W. Choi, E.Y. Park, S. Jeon, C. Kim, Clinical photoacoustic imaging platforms, Biomed. Eng. Lett. 8 (2018) 139–155, https://doi.org/10.1007/s13534-018-0062-7.
[6] M. Yang, L.Y. Zhao, X.J. He, N. Su, C. Zhao, H. Tang, T. Hong, W. Li, F. Yang, L. Lin, B. Zhang, R. Zhang, Y. Jiang, C. Li, Photoacoustic/ultrasound dual imaging of human thyroid cancers: an initial clinical study, Biomed. Opt. Exp. 8 (2017) 3449–3457, https://doi.org/10.1364/BOE.8.003449.
[7] J. Kim, S. Park, Y. Jung, S. Chang, J. Park, Y. Zhang, J.F. Lovell, C. Kim, Programmable real-time clinical photoacoustic and ultrasound imaging system, Sci. Rep. 6 (2016) 35137, https://doi.org/10.1038/srep35137.
[8] A. Garcia-Uribe, T.N. Erpelding, A. Krumholz, H. Ke, K. Maslov, C. Appleton, J. A. Margenthaler, L.V. Wang, Dual-modality photoacoustic and ultrasound imaging system for noninvasive sentinel lymph node detection in patients with breast cancer, Sci. Rep. 5 (2015) 15748, https://doi.org/10.1038/srep15748.
[9] E. Neuschler, R. Butler, C. Young, L.D. Barke, M.L. Bertrand, M. Böhm-Vélez, S. Destounis, P. Donlan, S.R. Grobmyer, J. Katzen, K.A. Kist, P.T. Lavin, E. V. Makariou, T.M. Parris, K.J. Schilling, F.L. Tucker, B.E. Dogan, A pivotal study of optoacoustic imaging to diagnose benign and malignant breast masses: a new evaluation tool for radiologists, Radiology 287 (2017) 398–412, https://doi.org/10.1148/radiol.2017172228.
[10] A. Becker, M. Masthoff, J. Claussen, S.J. Ford, W. Roll, M. Burg, P.J. Barth, W. Heindel, M. Schäfers, M. Eisenblätter, M. Wildgruber, Multispectral optoacoustic tomography of the human breast: characterisation of healthy tissue and malignant lesions using a hybrid ultrasound-optoacoustic approach, Eur. Radiol. 28 (2017) 602–609, https://doi.org/10.1007/s00330-017-5002-x.
[11] C. Lee, W. Choi, J. Kim, C. Kim, Three-dimensional clinical handheld photoacoustic/ultrasound scanner, Photoacoustics 18 (2020) 100173, https://doi.org/10.1016/j.pacs.2020.100173.
[12] A.A. Oraevsky, B. Clingman, J. Zalev, A.T. Stavros, W.T. Yang, J.R. Parikh, Clinical optoacoustic imaging combined with ultrasound for coregistered functional and anatomical mapping of breast tumors, Photoacoustics 12 (2018) 30–45, https://doi.org/10.1016/j.pacs.2018.08.003.
[13] L.V. Wang, H.I. Wu, Biomedical Optics: Principles and Imaging, John Wiley & Sons Inc., New Jersey, 2012.
[14] C. Zhu, Q. Liu, Review of Monte Carlo modeling of light transport in tissues, J. Biomed. Opt. 18 (2013), 50902, https://doi.org/10.1117/1.JBO.18.5.050902.
[15] T. Durduran, R. Choe, W.B. Baker, A.G. Yodh, Diffuse optics for tissue monitoring and tomography, Rep. Prog. Phys. 73 (2010), 076701, https://doi.org/10.1088/0034-4885/73/7/076701.
[16] T. Saratoon, T. Tarvainen, B.T. Cox, S.R. Arridge, A gradient-based method for quantitative photoacoustic tomography using the radiative transfer equation, Inverse Probl. 29 (2013), 075006, https://doi.org/10.1088/0266-5611/29/7/075006.
[17] S. Tzoumas, V. Ntziachristos, Spectral unmixing techniques for optoacoustic imaging of tissue pathophysiology, Philos. Trans. Math. Phys. Eng. Sci. 375 (2017) 0262, https://doi.org/10.1098/rsta.2017.0262.
[18] S. Tzoumas, A. Nunes, I. Olefir, S. Stangl, P. Symvoulidis, S. Glasl, C. Bayer, G. Multhoff, V. Ntziachristos, Eigenspectra optoacoustic tomography achieves quantitative blood oxygenation imaging deep in tissues, Nat. Commun. 7 (2016), 12121, https://doi.org/10.1038/ncomms12121.
[19] I. Olefir, S. Tzoumas, C. Restivo, P. Mohajerani, L. Xing, V. Ntziachristos, Deep learning based spectral unmixing for optoacoustic imaging of tissue oxygen saturation, IEEE Trans. Med. Imaging (2020), 3001750, https://doi.org/10.1109/TMI.2020.3001750.
[20] C.J. Cai, K.X. Deng, C. Ma, J.W. Luo, End-to-end deep neural network for optical inversion in quantitative photoacoustic imaging, Opt. Lett. 43 (2018) 2752–2755, https://doi.org/10.1364/OL.43.002752.
[21] C. Bench, A. Hauptmann, B.T. Cox, Toward accurate quantitative photoacoustic imaging: learning vascular blood oxygen saturation in three dimensions, J. Biomed. Opt. 25 (2020), 085003, https://doi.org/10.1117/1.JBO.25.8.085003.
[22] P.C. Beard, J.G. Laufer, B.T. Cox, S.R. Arridge, Quantitative photoacoustic imaging: measurement of absolute chromophore concentrations for physiological and molecular imaging, in: B.R. Masters, L.V. Wang (Eds.), Photoacoustic Imaging and Spectroscopy, Taylor and Francis, Abingdon, 2009, pp. 121–143.
[23] C. Xu, P.D. Kumavor, A. Aguirre, Q. Zhu, Investigation of a diffuse optical measurements-assisted quantitative photoacoustic tomographic method in reflection geometry, J. Biomed. Opt. 17 (2012), 061213, https://doi.org/10.1117/1.JBO.17.6.061213.
[24] X. Lei, H. Jiang, Integrated photoacoustic and diffuse optical tomography system for imaging of human finger joints in vivo, J. Biophotonics 9 (2016) 213–217, https://doi.org/10.1002/jbio.201500197.
[25] M. Li, Y. Tang, J. Yao, Photoacoustic tomography of blood oxygenation: a mini review, Photoacoustics 10 (2018) 65–73, https://doi.org/10.1016/j.pacs.2018.05.001.
[26] L.Y. Zhao, M. Yang, Y.X. Jiang, C.H. Li, Optical fluence compensation for handheld photoacoustic probe: An in vivo human study case, J. Innov. Opt. Health Sci. 10 (2017) 1740002, https://doi.org/10.1142/S1793545817400028.
[27] S.H. Tseng, A. Grant, A.J. Durkin, In vivo determination of skin near-infrared optical properties using diffuse optical spectroscopy, J. Biomed. Opt. 13 (2008) 014016, https://doi.org/10.1117/1.2829772.
[28] P. Taroni, A. Bassi, D.C.A. Farina, R.C.A. Pifferi, Diffuse optical spectroscopy of breast tissue extended to 1100 nm, J. Biomed. Opt. 14 (2009) 054030, https://doi.org/10.1117/1.3251051.
[29] D. Grosenick, H. Wabnitz, K.T. Moesta, J. Mucke, P.M. Schlag, H. Rinneberg, Time-domain scanning optical mammography: II. Optical properties and tissue parameters of 87 carcinomas, Phys. Med. Biol. 50 (2005) 2451–2468, https://doi.org/10.1088/0031-9155/50/11/002.
[30] V.G. Peters, D.R. Wyman, M.S. Patterson, G.L. Frank, Optical properties of normal and diseased human breast tissues in the visible and infrared, Phys. Med. Biol. 35 (1990) 1317–1334, https://doi.org/10.1088/0031-9155/35/9/010.
[31] H. Heusmann, J. Koelzer, G. Mitic, Characterization of female breasts in vivo by time-resolved and spectroscopic measurements in the near infrared spectroscopy, J. Biomed. Opt. 1 (1996) 425–434, https://doi.org/10.1117/12.250669.
[32] E. Maneas, W.F. Xia, O. Ogunlade, M. Fonseca, D.I. Nikitichev, A.L. David, S. J. West, S. Ourselin, J.C. Hebden, T. Vercauteren, A.E. Desjardins, Gel wax-based tissue-mimicking phantoms for multispectral photoacoustic imaging, Biomed. Opt. Express 9 (2018) 1151–1163, https://doi.org/10.1364/BOE.9.001151.
[33] M. Fonseca, E. Malone, F. Lucka, R. Ellwood, L. An, S. Arridge, P. Beard, B. Cox, Three-dimensional photoacoustic imaging and inversion for accurate quantification of chromophore distributions, Proc. SPIE. Int. Soc. Opt. Eng. (2017), 10064, https://doi.org/10.1117/12.2250964.
[34] H.G. Akarçay, S. Preisser, M. Frenz, J. Rička, Determining the optical properties of a gelatin-TiO2 phantom at 780 nm, Biomed. Opt. Express 3 (2012) 418–434, https://doi.org/10.1364/BOE.3.000418.
[35] Oregon Medical Laser Center, Tabulated Molar Extinction Coefficient for ICG and Intralipid in Water, 1998 (Accessed 20 June 2020), http://omlc.org/spectra/index.html.
[36] P.D. Ninni, F. Martelli, G. Zaccanti, Intralipid: towards a diffusive reference standard for optical tissue phantoms, Phys. Med. Biol. 56 (2011) N21–N28, https://doi.org/10.1088/0031-9155/56/2/N01.
[37] M. Yang, L.Y. Zhao, F. Yang, M. Wang, N. Su, C.Y. Zhao, Y. Gui, Y. Wei, R. Zhang, J. C. Li, T. Han, X.J. He, L. Zhu, H.W. Wu, C.H. Li, Y.X. Jiang, Quantitative analysis of breast tumors aided by three-dimensional photoacoustic/ultrasound functional imaging, Sci. Rep. 10 (2020) 8047, https://doi.org/10.1038/s41598-020-64966-6.

Tao Han received his Ph.D. degree in the Chemical Engineering Department from Loughborough University in 2016. He is currently a postdoctoral research fellow at Department of Biomedical Engineering in Peking University. His research interest includes photoacoustic imaging, multi-modality imaging, and currently focuses on quantitative photoacoustic breast imaging.

Meng Yang is senior physician and associate professor in Ultrasonography Department, Peking Union Medical College Hospital. She received her M.D. degree in Medical Imaging and Nuclear Medicine from Peking Union Medical College Hospital in 2013. She is an expert in superficial, musculoskeletal, Obstetric and Gynecologic ultrasonography. Her research interest focuses on the clinical translation of photoacoustic functional imaging, molecular imaging and multi-modality imaging for clinical diagonsis.

Fang Yang received her Ph.D. degree in the Biomedical Engineering Department, Tianjin University, 2006. She is currently a senior engineer in Mindray Bio-Medical Electronics Co.,Ltd., Shenzhen. She is focusing on the development of ultrasound/photoacoustics dual modality imaging system for clinical use.

Lingyi Zhao is a PhD candidate in the Peking University/Georgia Tech/Emory BME joint PhD program. She focuses on developing medical imaging device and processing imaging data from clinical studies, particularly in photoacoustic imaging and shear wave imaging.

Yuxin Jiang is chief physician and professor in Ultrasonography Department, Peking Union Medical College Hospital. He is the vice president of Chinese Medical Doctor Association, chairman of the Chinese Medical Association (Ultrasonography branch) and committee member of International Society of Ultrasound in Obstetrics and Gynecology (ISUOG). Professor Yuxin Jiang is also the vice president of Asian Federation of Societies for Ultrasound in Medicine and Biology (AFSUMB). He has authored over 100 peer-review journal articles and served as the chief editor of Chinese Journal of Ultrasonography and Chinese Journal of Medical Imaging Technology. His research is focused on ultrasonic contrast, intravenous ultrasound, early stage diagnosis of breast cancer, ultrasound in obstetrics and gynecology.

Changhui Li is an associate professor in the department of Biomedical Engineering of Peking University. He received his B.Sc. degree in 1997 from Peking University and Ph.D. degree in 2006 from Texas A&M University. Prior to joining Peking University, he worked at Washington University, St. Louis as a post doctor from 2006 to 2010. His research focuses on developing novel biomedical imaging methods, including photoacoustic imaging and fluorescence imaging.